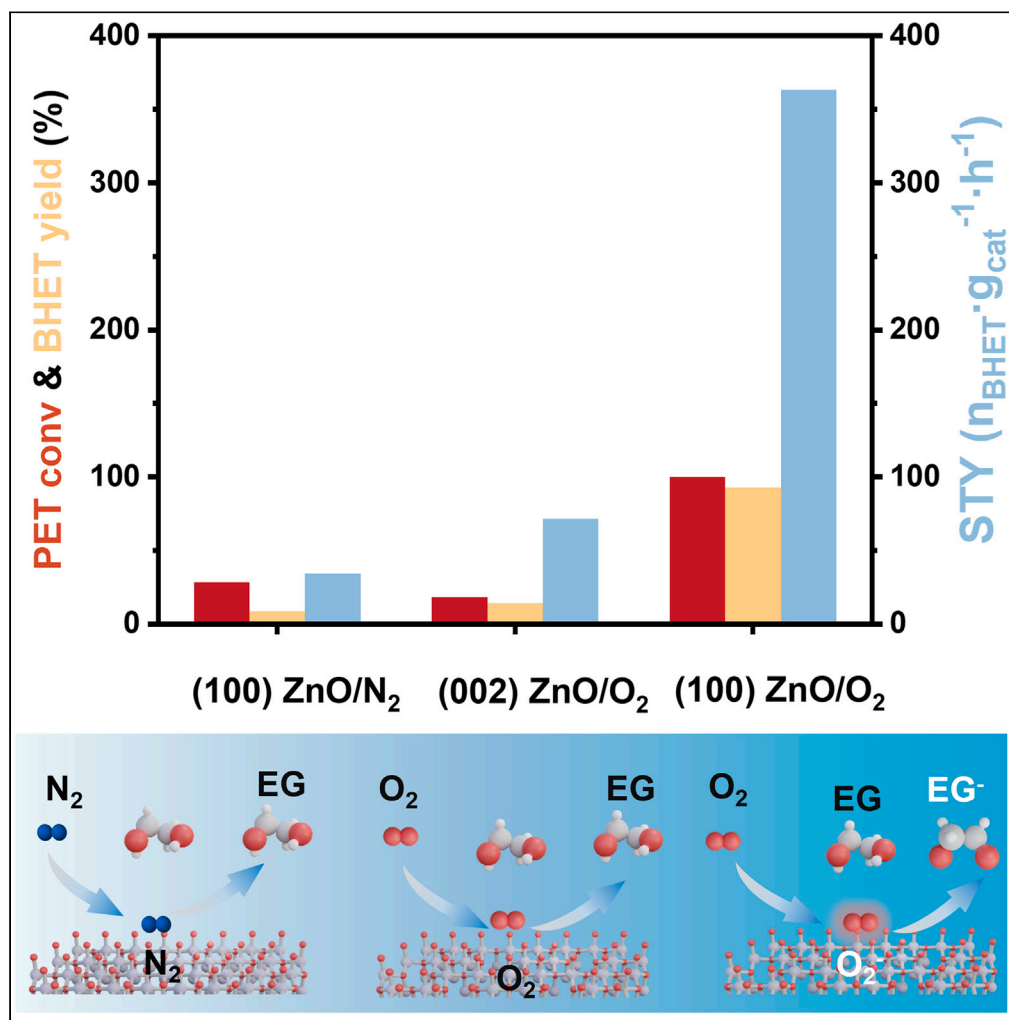


Article

Molecular oxygen-assisted in defect-rich ZnO for catalytic depolymerization of polyethylene terephthalate



Jingjing Cao,
Yuheng Lin,
Tianpeng Zhou,
Wei Wang,
Quanxing Zhang,
Bingcai Pan, Wei
Jiang

bcpan@nju.edu.cn (B.P.)
jiangwei@nju.edu.cn (W.J.)

Highlights

Defect-rich ZnO NSs exhibit outstanding catalytic activity for PET depolymerization

Gram-scale of PET and mixed PET plastic for depolymerization

Catalytic transesterification of O₂-assisted defect-rich ZnO NSs

Cao et al., iScience 26, 107492
August 18, 2023 © 2023 The
Authors.
<https://doi.org/10.1016/j.isci.2023.107492>

Article

Molecular oxygen-assisted in defect-rich ZnO for catalytic depolymerization of polyethylene terephthalate

Jingjing Cao,¹ Yuheng Lin,¹ Tianpeng Zhou,¹ Wei Wang,² Quanxing Zhang,¹ Bingcai Pan,^{1,*} and Wei Jiang^{1,3,*}

SUMMARY

Polyethylene terephthalate (PET) is the most produced polyester plastic; its waste has a disruptive impact on the environment and ecosystem. Here, we report a catalytic depolymerization of PET into bis(2-hydroxyethyl) terephthalate (BHET) using molecule oxygen (O₂)⁻ assisted in defect-rich ZnO. At air, the PET conversion rate, the BHET yield, and the space-time yield are 3.5, 10.6, and 10.6 times higher than those in nitrogen, respectively. Combining structural characterization with the results of DFT calculations, we conclude that the (100) facet of defect-rich ZnO nanosheets conducive to the formation of reactive oxygen species (*O₂⁻) and Zn defect, promotes the PET breakage of the ester bond and thus complete the depolymerization processed. This approach demonstrates a sustainable route for PET depolymerization by molecule-assisted defect engineering.

INTRODUCTION

Polyethylene terephthalate (PET) is the most produced polyester plastic in the world. It is used in plastic bottles, food containers, carpet fibers, etc.¹ However, most post-consumer PET is considered garbage, which is then landfilled or discarded in nature, leading to serious environmental pollution.^{2–4} To date, only 7–10% of annually produced PET bottles are reclaimed, thus necessitating effective strategies for its recycling. Chemical recycling is the most common and effective method, major recycling strategies (e.g., pyrolysis, hydrolysis, glycolysis, aminolysis, and hydrogenation)^{5–9} have been developed to decompose PET into their recyclable monomers. Glycolysis is a promising recycling method in the chemical recovery of PET, due to its low cost and efficient conversion of depolymerization.^{10–13} However, disadvantages of homogeneous catalysts and other issues, such as low selectivity (yield < 70%) or metal residue, limit their application in the recycling of PET (Scheme 1).^{14–18} The development of low-cost catalysts with high activity, high selectivity, and high stability remains a challenge in the process of PET depolymerization.

Heterogeneous catalysts have the advantage of being easy to separate, and heterogeneous catalytic systems possess great prospects for the bulk transformation of chemicals. Heterogeneous catalysts have been studied as promising candidates for catalyzing the glycolysis of PET (Scheme 1),^{11,12,19,20} such as metal oxides and nano-oxides (γ -Fe₂O₃, Si-TEA, MWCNTs/Fe₃O₄, ZnO, Co NPs, CeO₂), POMs (K₆SiW₁₁-ZnO₃₉(H₂O), solid base and acid (β -Zeolite, SO₄²⁻/Co/ZnO), and MOFs (ZIF-8, MAF-6), Na₁₂[WZnM₂(H₂O)₂(ZnW₉O₃₄)₂]. Till now, the reported ZnO-based catalysts for PET glycolysis are not satisfactory in terms of reaction activity and selectivity.^{21,22} For example, ZnO nanoparticles catalyzed the glycolysis of PET into bis(hydroxyethyl) terephthalate (BHET) monomer yield < 10% at 180°C in N₂ atmosphere and at 1 atm. Even at high temperatures (e.g., 260°C) and under high pressure (5 MPa), the BHET monomer yield could only reach 67%. Questions, such as which crystal facet is active and whether crystal defect affects catalytic activity, remain unanswered. So far, there are only a few studies with non-conclusive results that have addressed these problems.

Recently, defects engineering on metal oxide surfaces would influence surface states (e.g., chemical reactivity, electronic structure, crystal plane, etc)²³ to improve catalytic performance. Defect-rich metal oxides have found their way into applications concerning hydrogen production,²⁴ methane conversion,^{25,26} lithium reduction,²⁷ water splitting,²⁸ ammonia synthesis,²⁹ supercapacitors,³⁰ and carbon dioxide electro-reduction.^{31–33} Defect-rich metal oxides often exhibit superior catalytic performance over their original

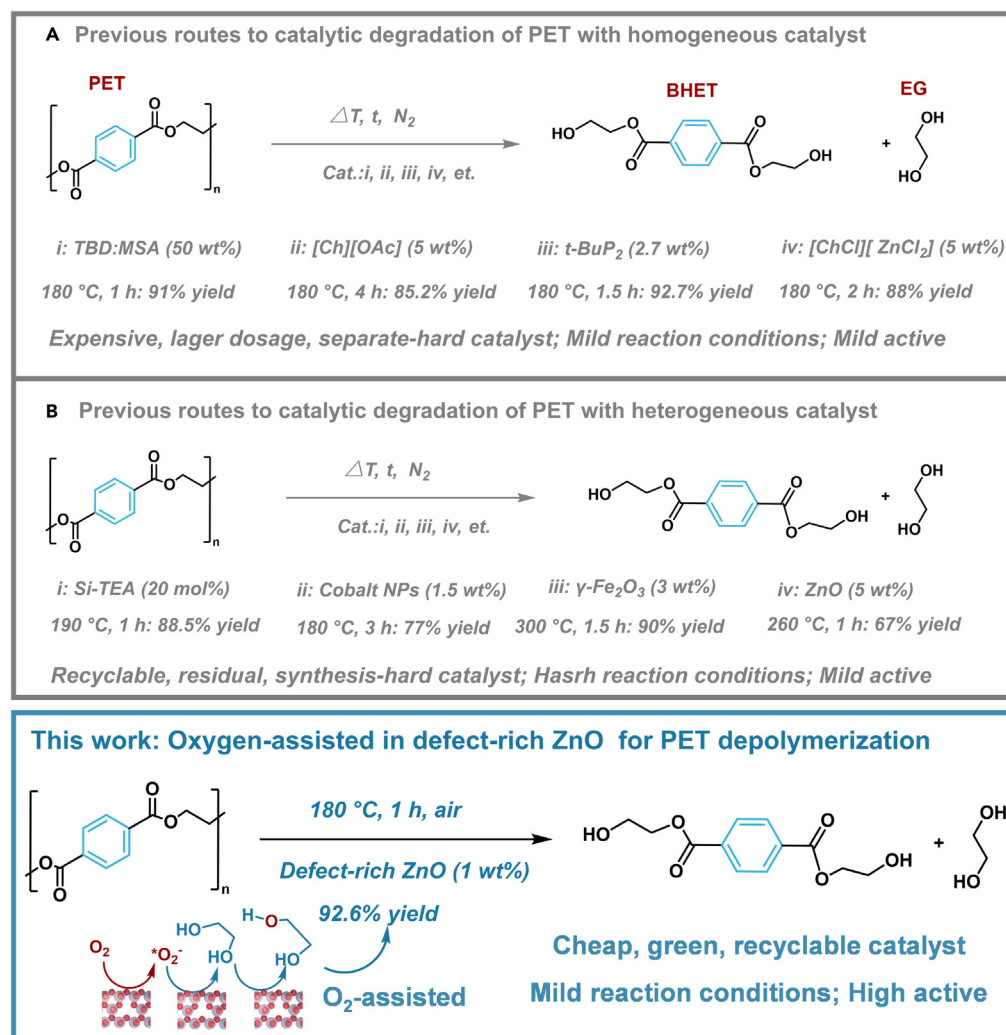
¹State Key Laboratory of Pollution Control and Resources Reuse, National Engineering Research Center for Organic Pollution Control and Resource Reuse, School of the Environment, Nanjing University, Nanjing 210023, China

²Department of Chemistry and Centre for Pharmacy, University of Bergen, 5007 Bergen, Norway

³Lead contact

*Correspondence: bcpan@nju.edu.cn (B.P.), jiangwei@nju.edu.cn (W.J.)
<https://doi.org/10.1016/j.isci.2023.107492>





Scheme 1. Catalytic depolymerization of PET from the previous work and this work

form. While this type of defect-rich metal oxide catalyst holds great promise, it is still unknown whether it can effectively drive PET depolymerization.

Here, we systematically studied the influence of crystal morphology and active crystal surface of ZnO on PET glycolysis. Interestingly, we found that oxygen vacancies (O_v) and the catalytic environment (the presence of O_2) can significantly enhance the catalytic activity and improve BHET yield (Scheme 1). Among different crystal morphologies, the exposure of (100) facets to reaction media exhibited highly selective features for the PET conversion. We report PET conversion into BHET with high activity (yield = 92.6%, the STY was $363.2 n_{\text{BHET}} \cdot \text{g cat}^{-1} \cdot \text{h}^{-1}$) and good stability at 180°C in the presence of a defect-rich ZnO catalyst. Combining experimental evidence with the results of DFT calculations, we conclude that the key factor under PET depolymerization is the formation of reactive oxygen species ($^*O_2^-$) and Zn defect on the (100) facet of defect-rich ZnO. The results of this work guide the design of catalysts for PET recycling.

RESULTS AND DISCUSSION

Catalytic depolymerization of PET

The influences of ZnO nanosheets (NSs) in PET depolymerization were studied under nitrogen, oxygen, and air. The PET conversion rate (Conv), BHET yield (Yield), and space-time yield (STY) results are listed in Table 1. In nitrogen, the Conv of PET was 28.3%; the yield was 8.7%; the STY was $34.1 n_{\text{BHET}} \cdot \text{g cat}^{-1} \cdot \text{h}^{-1}$ (see Table 1, entry 1). When the reaction atmosphere changed to oxygen, these indicators improved

Table 1. Catalytic performance of different ZnO in PET conversion

Entry	Catalyst	Atmosphere	PET Conv (%)	BHET Yield (%) ^a	STY ($n_{\text{BHET}} \cdot \text{g}_{\text{cat}}^{-1} \cdot \text{h}^{-1}$)
1 ^b	ZnO NSs	N ₂	28.3	8.7	34.1
2 ^b	ZnO NSs	O ₂	100	92.6	363.2
3 ^b	ZnO NSs	air	100	92.4	362.8
4 ^b	ZnO rods (2 μm)	air	99.2	68.4	245.6
5 ^b	ZnO NRs (200 nm)	air	100	82.8	325.4
6 ^b	ZnO NRs (90 nm)	air	100	89.18	350.1
7 ^b	ZnO NRs (50 nm)	air	100	91.2	357.2
8 ^b	ZnO NSs-200°C	air	40.5	13.2	51.8
9 ^b	ZnO NSs-400°C	air	61.5	42.3	166.2
10 ^b	ZnO NSs-500°C	air	54.6	38.1	149.7
11 ^b	MnO ₂	air	56.2	43.2	169.7
12 ^b	Co ₃ O ₄	air	55.8	47.7	184.7
13 ^b	CuO	air	45	32.5	127.2
14 ^b	Fe ₃ O ₄	air	16.3	3.6	14.1
15 ^b	NiO	air	19.2	10.2	40.1
16 ^b	Al ₂ O ₃	air	8.3	0.8	3.1
17 ^b	CeO ₂	air	13.5	6.1	23.9
18 ^b	None	air	6.8	0.6	/
19 ^c	ZnO NSs	air	100	90.5	363.2
20 ^b	ZnO NEs	air	36.1	30.5	119.7
21 ^b	ZnO NRs	air	45.6	42.5	167.1
22 ^b	ZnO rods	air	18.2	14.1	71.5

^aYields were determined by HPLC analysis of reaction mixtures relative to an internal standard. Please find the detail of the product analysis in the [supplemental information](#).

^bConditions: 1.0 g PET (white bottle), 4 g EG, Cat = 1 wt %, atmosphere, 180°C, 1 h.

^cConditions: 1.0 g PET (white, green purple, and light blue bottle), 4 g EG, Cat = 1 wt %, air, 180°C, 2 h (in [Table S3](#)).

significantly (Conv = 100%; Y = 92.6%; S = 363.2 $n_{\text{BHET}} \cdot \text{g}_{\text{cat}}^{-1} \cdot \text{h}^{-1}$) (see [Table 1](#), entry 2). The results of PET depolymerization in the air and oxygen were almost identical (see [Table 1](#), entry 3). These results indicated the oxygen molecules significantly promoted the depolymerization of PET.

We first systematically studied the effect of reaction conditions on the depolymerization of PET. With the increase of the reaction temperature from 160°C to 170°C, PET conv and BHET yield increased (see [Table S2](#), entry 1–2). At 180°C, the yield of BHET reached the maximum (92.6%). A further increase of the temperature to 190°C did not change the yield of BHET (see [Table S2](#), entry 3). The effect of the temperature could be explained by the reaction equilibrium between the BHET monomer and the oligomer. As to the effect of the reaction time, the maximum yield of BHET reached 92.6% after 60 min (see [Table S2](#), entries 4–6). Upon extending the reaction time to 90 min, the yield of BHET remained the same, where the reaction was in dynamic equilibrium. The number of active centers is directly linked to the amount of the catalyst. Therefore, PET conv and BHET yield increased rapidly when the catalyst dosage increased from 0.1 wt % to 1 wt % (see [Table S2](#), entries 7–8). The maximum yield of BHET was reached with the presence of 1 wt % ZnO. When the amount of ZnO was increased to 5 wt %, the yield remained unchanged (see [Table S2](#), entries 9–10). Based on these results, the optimal reaction conditions were found to be T = 180°C, t = 1 h, and the catalyst dose of 1 wt %. As mentioned previously, temperature is one of the key factors in PET glycolysis. Thus, the apparent activation energy was computed using the Arrhenius equation, which was found to be 148.5 kJ mol⁻¹, with a pre-exponential factor of 2×10^{15} ([Figure S7](#)).

We further examined how the size of ZnO particles affects the depolymerization of PET. We used ZnO particles with varied sizes (namely, 50 nm, 90 nm, and 200 nm, 2 μm) to carry out the glycolysis of PET. Under an

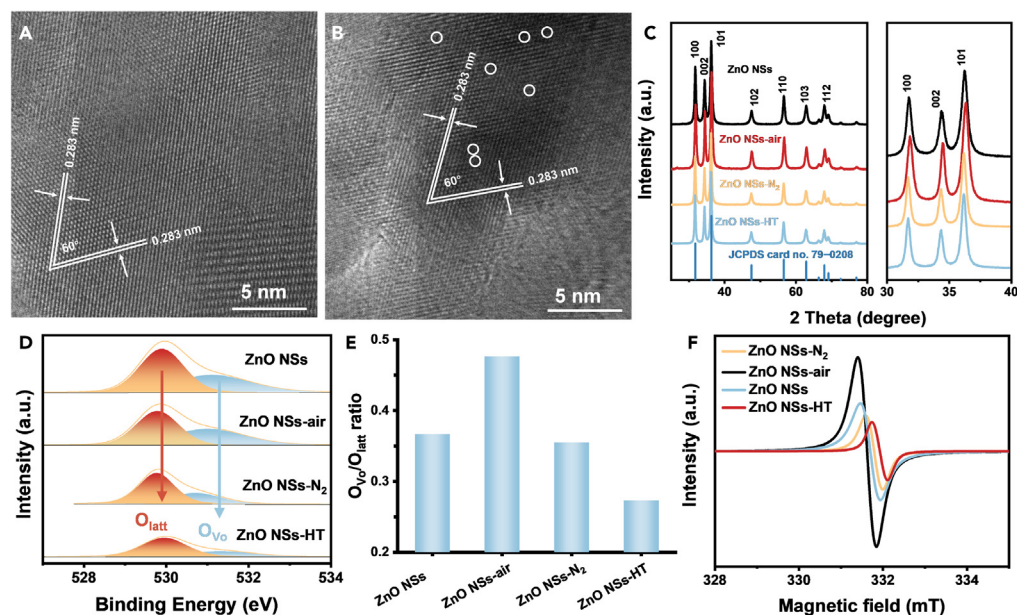


Figure 1. Structural characterizations for ZnO NSs, ZnO NSs-air, ZnO NSs-N₂, and ZnO NSs-HT

(A and B) HRTEM images of ZnO NSs, ZnO NSs-air.

(C) XRD spectra.

(D) O 1s XPS spectra.

(E) O_{Vo}/O_{latt} ratios.

(F) Room temperature ESR spectra.

atmosphere of the air, the PET conv, BHET yield, and the STY were found to be distinguished among these ZnO catalysts with varied sizes (Table 1, entries 4–7; Table S2, entries 11–18). These results strongly indicate that the size of ZnO is an influential factor in PET glycolysis. The synthesis methods of ZnO were investigated by comparing the effects of the morphology of ZnO on the depolymerization of PET. We compared the catalytic activities of ZnO NSs, ZnO nanospindles (NEs), ZnO nanorods (NRs), and ZnO rods (Figure S8). The catalytic activity of ZnO NSs showed the highest conversion of PET. The effects of calcination at different temperatures (namely, 200°C, 350°C, 400°C, and 500°C) on the catalytic reaction were studied by using the ZnO NSs (Table 1, entry 8–10). We found that the catalytic activity of ZnO calcined at 350°C was significantly higher than those at the other calcined temperatures.

Later, we compared the catalytic activity of ZnO NSs with other metal oxides (namely, MnO₂, Co₃O₄, CuO, Fe₃O₄, NiO, Al₂O₃, and CeO₂). We found that the catalytic activity of the ZnO NSs far exceeded that of the other metal oxide catalysts (Table 1, entries 11–19; Table S7).

The relationship between PET depolymerization and catalyst structure

To explore the relationship between PET depolymerization and ZnO NSs, we systematically studied the structure of ZnO. We synthesized dendritic ZnCO₃, which was treated with high-temperature pyrolysis to form ZnO NSs (Figures S10 and S11) under air and nitrogen atmospheres, denoted as ZnO NSs-air and ZnO NSs-N₂, respectively. Meanwhile, ZnO calcinated at 500°C is denoted as ZnO NSs-HT. The catalytic reaction was carried out using ZnO NSs as a model catalyst. The results of PET depolymerization performance in the ZnO NSs-air are optimal (see Table 1, entries 1–3, 10). Evidence in TEM and HRTEM images revealed the lattice fringes with a fringe spacing of 0.28 nm were ascribed to the (100) facets of hexagonal ZnO (Figures 1A and 1B; Figure S11).^{26,31} The crystal plane spacing and the corresponding dihedral angle (60°) of (100) and (010) facets indicated that ZnO NSs were in [001] orientation. The XRD patterns (Figure 1C) indicated that the ZnO NSs were a hexagonal phase (JCPDS card no. 79–0208).²⁶ Compared with XRD of ZnO NSs and ZnO NSs-air data, the (100), (002), and (101) peaks for ZnO NSs-HT tiny moved to lower angles in comparison to those peaks, meaning that lattice oxygen surface for saturated coordination. Raman spectra of all samples showed a hexagonal ZnO NSs Raman mode at 326, 371, and 433 cm⁻¹ (Figure S12).

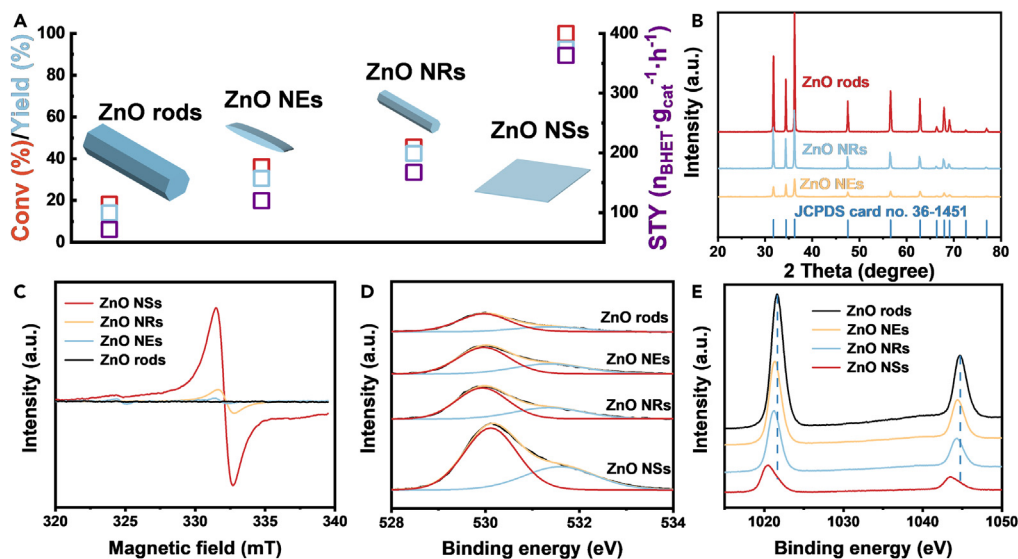


Figure 2. Catalytic performance and structural characterizations for ZnO rods, NEs, NRs, and NSs

- (A) Catalytic performance of ZnO rods, NEs, NRs, and NSs.
(B) XRD spectra.
(C) Room temperature ESR spectra.
(D) O 1s XPS spectra.
(E) Zn 2p XPS spectra.

A peak at 584 cm^{-1} was observed in Raman mode due to the presence of O_v in ZnO, in which the ZnO NSs-air more O_v than other samples.³⁴

The XPS spectra were calibrated with an indefinite carbon signal of 284.6 eV. XPS spectra of the Zn 2P region (Figure S13) showed two strong peaks at 1021.4 and 1044.5 eV, belonging to Zn $2p_{3/2}$ and $2p_{1/2}$ bands of Zn^{2+} species, respectively.³⁵ In the O 1s XPS spectra (Figure 1D), the two peaks at 529.5 and 531.3 eV corresponded to the lattice oxygen and O atoms near the O_v , respectively. The O 1s peak of the oxygen atom near O_v was the strongest in ZnO NSs-air, which also had the highest integral area ratio of O_v to lattice oxygen (Figure 1E). Further used analysis of electron paramagnetic resonance (ESR) spectra confirmed O_v levels. In Figure 1F, the peak strength of ZnO NSs-air was found to be much higher than that of other ZnO NSs in the case of $g = 1.958$.³⁶ In addition, photoluminescence (PL) spectra (Figure S14) showed that the luminescence peak of ZnO NSs-air at 435 nm was an electron-hole pair that can recombine at the site of vacancies. The peak strength of ZnO NSs-air was higher in other samples. In general, all the evidence confirmed that ZnO NSs-air had the highest O_v and defect level, indicating that the defect-rich surface is conducive to activating O_2 to generate oxygen species. We may conclude that a higher concentration of O_v and defect levels was indicative of higher activity in PET depolymerization.

To further explore the relationship between the ZnO of facet and PET depolymerization, we synthesized ZnO with defects on different facets. The depolymerization of PET performance over ZnO NSs significantly higher than ZnO rods, NEs, and NRs (Figure 2A and see Table 1, entry 1, 20–22). The structures of ZnO with different morphologies were characterized by SEM, TEM, and XRD. The diffraction peaks of ZnO NSs are attributed to hexagonal ZnO (JCPDS card no. 79–0208) (Figure 2B) and the diffraction peaks of ZnO rods, NRs, and NEs are attributed to wurtzite ZnO (JCPDS card No. 36–1451).^{37,38} In the HRTEM images (Figure S15), ZnO NSs showed continuous and ordered lattice fringes with a plane spacing of 0.283 nm corresponding to d100. The crystal plane spacing and the corresponding dihedral angle (60°) of (100) and (010) crystal planes indicated that ZnO nanosheets were in [001] orientation.²⁶ The lattice fringe of ZnO NRs is 0.26 nm, corresponding to d002 of the hexagonal ZnO.^{39,40}

To confirm whether O_v and defect levels of all ZnO samples are consistent with PET depolymerization activity, we utilized ESR signals strength to determine (Figure 2C). We conclude that the (100) facet of the ZnO NSs had the highest O_v and defect level. By comparing the PL intensity of ZnO in different morphologies

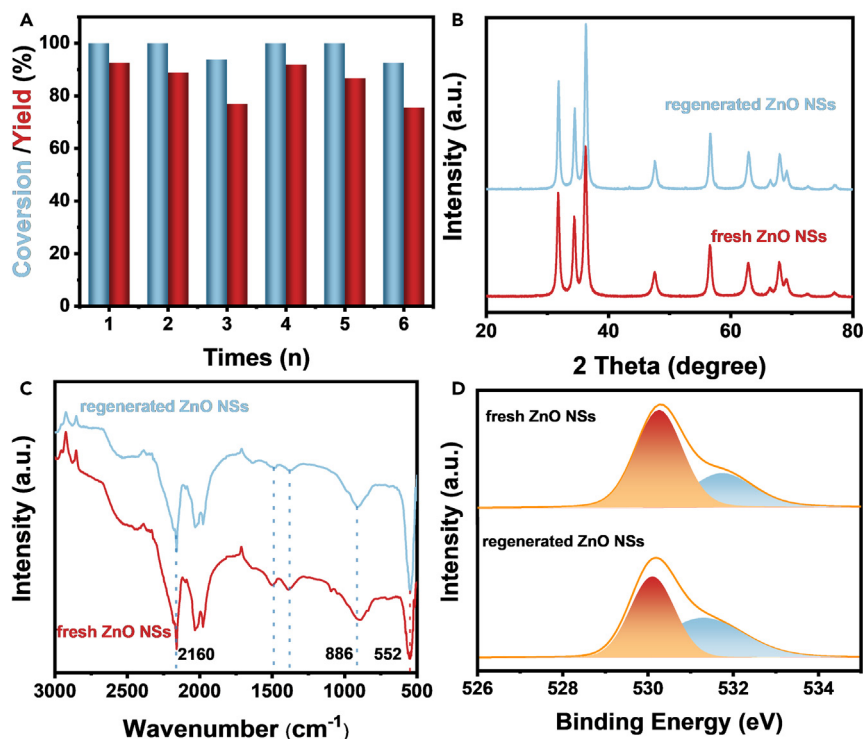


Figure 3. Characterization of the fresh ZnO NSs and regenerated ZnO NSs after 3 catalytic cycles

(A) Stability of the catalyst.
(B) XRD spectra.
(C) FTIR spectra.
(D) The O 1s XPS spectra.

(Figure S16), we find that the ZnO NSs had the highest O_v and defect level, which was consistent with the analysis of ESR. In the O 1s XPS spectra (Figure 2D), the ZnO NSs have a larger peak area among the samples, which is indicative of a higher O_v concentration. According to the Zn 2p orbital spectrum in Figure 2E, Zn 2p_{3/2} and Zn 2p_{1/2} are located at 1020.5 and 1043.6 eV, respectively, which indicates that Zn existed in the bivalent form. With an increase in the O_v concentration, the binding energy of Zn 2p_{1/2} and Zn 2p_{3/2} shifted to the lower binding energy, indicating that increased the electron density of Zn atoms.^{41,42} In general, the evidence in the characterizations confirmed that the (100) facet of defect-rich ZnO NSs had the highest O_v and defect level, providing significantly more active sites and oxygen species for PET depolymerization.

Catalyst stability and recycling of other PET waste

The results showed that the catalytic performance of reused ZnO NSs decreased after the third cycle (Figure 3A). The problem of catalytic sintering can be solved by regeneration. The regeneration process is presented in the STAR Methods section. The catalytic activity of deactivated ZnO NSs almost recovered to its original level. In TEM images, FTIR patterns, and XRD patterns (Figures 3B, 3C, S17, and Table S3), the regenerated ZnO NSs showed an identical structure and the same phase structure as the fresh ZnO NSs, which might be identified as the reason behind the stable high PET conversion and BHET yield of the regenerated ZnO NSs. According to the high-resolution O 1s XPS spectrum (Figure 3D), the O_v concentration of regenerated ZnO NSs remained unchanged. Defect-rich ZnO NSs are also effective in catalytic process conversion of post-consumption PET products, e.g., packing bags, water bottles, sprite bottles, polyester fibers, carpets, and mineral water bottles with polypropylene mixtures. For these, the yield of BHET was 92.4%, 91.2%, 90.7%, 90.4%, 85.6%, and 90.2%, respectively, after reaction at 180°C for 1–2 h (Figure S18), indicating that the effect of any processed/stabilized plastic additive on the catalytic process was negligible.

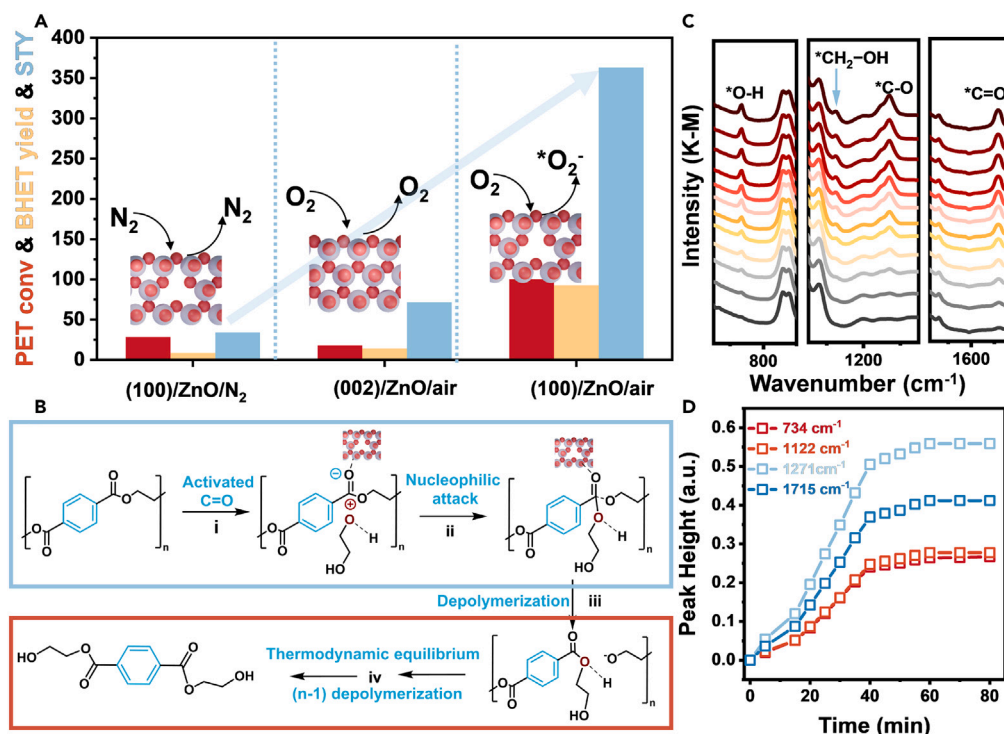


Figure 4. Catalytic depolymerization path

(A) A catalytic performance for different facets and atmospheres of ZnO NSs.

(B) A plausible pathway for ZnO NSs catalytic degradation of PET.

(C) *In situ* FTIR spectra of the PET depolymerization on ZnO NSs.

(D) Normalized intensities of the typical surface functional groups including *C=O (~1715 cm⁻¹), *C–O (1271 cm⁻¹), *CH₂–OH (1122 cm⁻¹), and *O–H (734 cm⁻¹) with various reaction times. Conditions: 1.0 g PET, 4 g EG, Cat = 1 wt %, atmosphere, 180°C, 80 min.

Catalytic depolymerization path and mechanism

To unravel the inherent reasons for the improved performance in PET depolymerization, how would O_v concentration and the facet of ZnO NSs affect the PET depolymerization process? The catalytic results showed that the (100) facet of ZnO NSs with high O_v concentration was significantly higher than the (002) facet of ZnO or (100) facet of ZnO–N₂ NSs (Figure 4A). Therefore, we propose a reaction path for PET depolymerization by ZnO NSs (Figure 4B). In step (i), O₂ is adsorbed on the surface of defect-rich ZnO NSs. In the process of heating, O₂ preferentially aggregates on Zn sites and O_v of ZnO (100) facet, forming a large number of oxygen species.^{31,43} The ZnO surface produces more O_v. Hydroxyl groups of ethylene glycol (EG) interact with oxygen species. This deprotonates ethylene glycol (EG⁻) and makes it more nucleophilic. In step (ii), the unsaturated coordinated Zn atoms on the surface of ZnO are more likely to interact with the carbonyl oxygen of PET, making the carbonyl carbon capable of carrying more positive charges. In step (iii), the EG⁻ acts as a nucleophile, thus attacking the carbonyl carbon, and breaking the C–O bonds of PET. In step (iv), the EG⁻ and the carbonyl carbon form a new chemical bond, and simultaneously the EG⁻ and the carbonyl oxygen separate from the catalyst surface to complete a catalytic cycle.

To further investigate the reaction pathway, *in situ* Fourier transform infrared spectroscopy (FTIR) characterize were applied to detect the reaction intermediates catalytic depolymerization of ZnO NSs (Figures 4C, 4D, and S19). The PET depolymerization was a reaction to an air atmosphere at 180°C for 80 min. As the reaction proceeded, a new peak at 1715 cm⁻¹ was observed and their peak intensities visibly increased along the progress of the reaction. Both the increased peaks could be attributed to the vibrations of *C=O group. In the meantime, the peaks at 1,271 cm⁻¹ were also detected, which could be ascribed to the asymmetric *C–O group, while the peaks at 1,122 and 734 cm⁻¹ could be contributed to *CH₂–OH group and *O–H, respectively. These functional groups are characteristics of the intermediate products in the depolymerization of PET, and the intensity of these peaks increased as the reaction

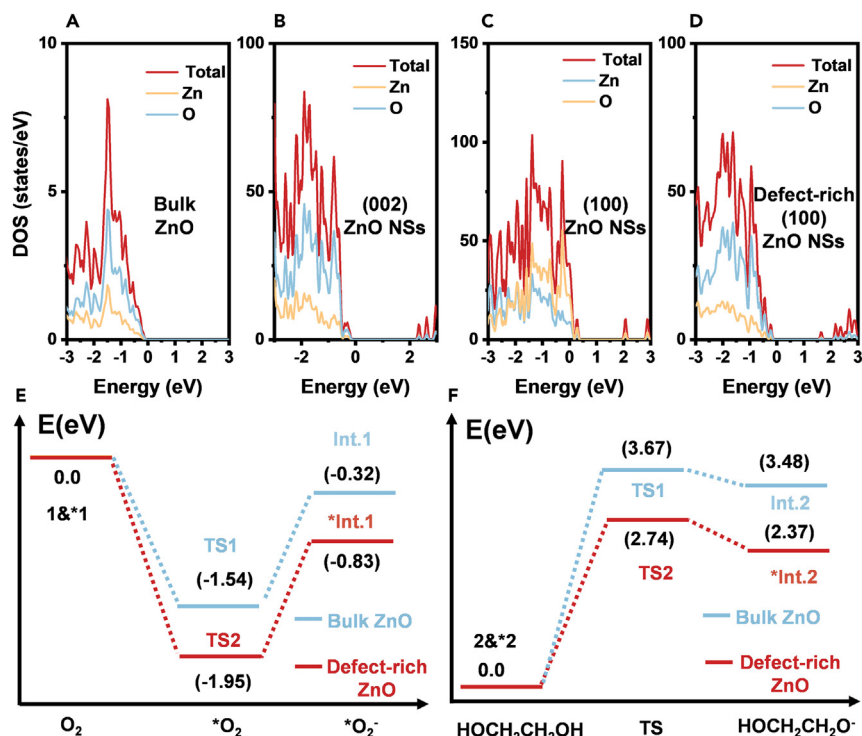


Figure 5. Calculated the density of state (DOS) and Gibbs free energy changes

(A–D) The density of states (DOS) of bulk ZnO, ZnO (002) slab, ZnO (100) slab, and defect-rich ZnO (100) slab.

(E) The free energy profiles for $*O_2 \rightarrow *O_2^-$ on bulk ZnO and defect-rich ZnO slabs.

(F) The free energy profiles for $HOCH_2CH_2OH \rightarrow *OCH_2CH_2OH$ on bulk ZnO and defect-rich ZnO slabs.

continued. The *in situ* infrared data confirmed the path of PET conversion on the surface of defect-rich ZnO NSs, and the results are highly consistent with the experimental results.

To further understand the mechanism of PET depolymerization, we calculated the density of state (DOS) on different crystal planes by density functional theory (DFT). Compared with bulk ZnO, the (002) facet, (100) facet, and defect-rich (100) facet showed an increase of DOS around the valence band edge, where the increase of charge density came from Zn and oxygen atoms. The electrons are more likely to gather near the valence band of ZnO with O_v , and a new defect level appeared near the valence band, compared with that of the (100) crystal plane without O_v . The presence of O_v led to the exposure of a large number of unsaturated Zn atoms, which effectively interacted with oxygen in the adjacent plane and generated more active electrons on the catalyst surface.

In addition, we calculated Gibbs free energy changes of ZnO NSs-activated O_2 and EG (Figure 5; Tables S4–S6). The PET depolymerization rate-determining steps (RDS) are $*O_2 \rightarrow *O_2^-$ and $HOCH_2CH_2OH \rightarrow *OCH_2CH_2OH$.⁴⁴ When comparing the energy barriers of different RDS, the catalytic activity of defect-rich ZnO was found to be much higher than that of the bulk ZnO for the transition processes of $*O_2 \rightarrow *O_2^-$ and $HOCH_2CH_2OH \rightarrow *OCH_2CH_2OH$ (Figures 5E, 5F, S20, and S21). The energy barrier of the defect-rich ZnO NSs is 1.02 eV and 2.37 eV for the formation of $*O_2^-$ and $*OCH_2CH_2OH$ intermediates, respectively. These values are much lower than those of bulk ZnO (1.22 eV and 3.48 eV). The low energy barrier is attributed to the presence of abundant surface O_v , efficiently generating active O_2^- species. Thus, the O_2^- species attack hydroxyl groups in ethylene glycol to form $*OCH_2CH_2OH$. Zn sites on the surface of the catalyst activate the carbonyl oxygen of the oligomer, which is further decomposed into BHET.

Conclusions

In summary, to achieve stable and efficient catalytic depolymerization of PET, we have developed a method via precise cleavage ester bonds of PET on an O_2 -assisted ZnO NSs catalyst to obtain high-yield BHET. The

experimental results show that the reaction atmosphere and crystal planes can all affect PET depolymerization. Essentially, these factors exert their influence by adjusting the defect structure and O_v concentration of the ZnO NSs. The characterization results and DFT calculation confirm that the high-charge density on the surface of (100) ZnO NSs resulted in a higher concentration of O_v , which leads to the hybridization of Zn and O atoms adjacent to the surface of ZnO NSs to form defect. Based on all the experimental results and DFT calculations, Zn atoms with a higher concentration of O_v and unsaturated coordination function as active sites for the activation of EG and PET, significantly improving the performance of PET depolymerization. This work elucidates the role of O_2 and defect-rich ZnO NSs in the depolymerization of PET waste, breaking through the traditional catalysis requiring N_2 in PET depolymerization, providing a new approach for the design of efficient catalysts for PET waste depolymerization.

Limitations of the study

In this work, we designed and prepared O_2 -assisted ZnO NSs to promote the conversion of PET. This work elucidates the role of O_2 and defect-rich ZnO NSs in the depolymerization of PET waste, breaking through the traditional catalysis requiring N_2 in PET depolymerization. However, the understanding and study of the reaction mechanism still need to be further deepened. Future works need to be more *in-situ* characterization methods proving mechanisms.

STAR★METHODS

Detailed methods are provided in the online version of this paper and include the following:

- KEY RESOURCES TABLE
- RESOURCE AVAILABILITY
 - Lead contact
 - Materials availability
 - Data and code availability
- METHOD DETAILS
 - Materials
 - Synthesis of ZnO NSs
 - Synthesis of ZnO NRs
 - Synthesis of ZnO NEs
 - Evaluation of the catalytic glycolysis of PET with ZnO
 - Carbon balance
 - Catalyst recycling
 - Catalyst of characterization
 - Analysis of starting materials and products
 - DFT calculation details

SUPPLEMENTAL INFORMATION

Supplemental information can be found online at <https://doi.org/10.1016/j.isci.2023.107492>.

ACKNOWLEDGMENTS

This research was supported by The National Key Research and Development Program of China (YFC20181901404). We thank Prof. Shimei Xu for their support of *in situ* infrared measurement. Gratitude is expressed to Dr. Xiaodong Li for support of theoretical calculation.

AUTHOR CONTRIBUTIONS

J.C.: Experiments perform, Formal analysis, Writing-original draft. W.W.: Formal analysis, Graphic design, writing. T.Z. and Y.L.: Formal analysis. B.P. and Q.Z.: Conceptualization, Result analysis. W.J.: Conceptualization, Formal analysis, Funding acquisition, Resources, Supervision.

DECLARATION OF INTERESTS

The authors declare no competing interests.

INCLUSION AND DIVERSITY

We support inclusive, diverse, and equitable conduct of research.

Received: March 7, 2023

Revised: March 22, 2023

Accepted: July 23, 2023

Published: July 27, 2023

REFERENCES

- Geyer, R., Jambeck, J.R., and Law, K.L. (2017). Production, use, and fate of all plastics ever made. *Sci. Adv.* 3, e1700782. <https://doi.org/10.1126/sciadv.1700782>.
- Sardon, H., and Dove, A.P. (2018). Plastics recycling with a difference. *Science* 360, 380–381. <https://doi.org/10.1126/science.aat4997>.
- Law, K.L., and Thompson, R.C. (2014). Microplastics in the seas. *Science* 345, 144–145. <https://doi.org/10.1126/science.1254065>.
- Rochman, C.M., Browne, M.A., Halpern, B.S., Hentschel, B.T., Hoh, E., Karapanagioti, H.K., Rios-Mendoza, L.M., Takada, H., Teh, S., and Thompson, R.C. (2013). Classify plastic waste as hazardous. *Nature* 494, 169–171. <https://doi.org/10.1038/494169a>.
- Ragaert, K., Delva, L., and Van Geem, K. (2017). Mechanical and chemical recycling of solid plastic waste. *Waste Manag.* 69, 24–58. <https://doi.org/10.1016/j.wasman.2017.07.044>.
- Kratish, Y., Li, J., Liu, S., Gao, Y., and Marks, T.J. (2020). Polyethylene terephthalate deconstruction catalyzed by a carbon-supported single-site molybdenum-dioxo complex. *Angew. Chem. Int. Ed.* 59, 19857–19861. <https://doi.org/10.1002/anie.202007423>.
- Westhues, S., Idel, J., and Klankermayer, J. (2018). Molecular catalyst systems as key enablers for tailored polyesters and polycarbonate recycling concepts. *Sci. Adv.* 4, eaat9669. <https://doi.org/10.1126/sciadv.aat9669>.
- Rahimi, A., and García, J.M. (2017). Chemical recycling of waste plastics for new materials production. *Nat. Rev. Chem.* 1, 0046. <https://doi.org/10.1038/s41570-017-0046>.
- Vollmer, I., Jenks, M.J.F., Roelands, M.C.P., White, R.J., van Harmelen, T., de Wild, P., van der Laan, G.P., Meirer, F., Keurentjes, J.T.F., and Weckhuysen, B.M. (2020). Beyond mechanical recycling: Giving new life to plastic waste. *Angew. Chem. Int. Ed.* 59, 15402–15423. <https://doi.org/10.1002/anie.201915651>.
- Rorrer, N.A., Nicholson, S., Carpenter, A., Biddy, M.J., Grundl, N.J., and Beckham, G.T. (2019). Combining reclaimed PET with bio-based monomers enables plastics upcycling. *Joule* 3, 1006–1027. <https://doi.org/10.1016/j.joule.2019.01.018>.
- Zhang, M.-Q., Wang, M., Sun, B., Hu, C., Xiao, D., and Ma, D. (2022). Catalytic strategies for upvaluing plastic wastes. *Chem* 8, 2912–2923. <https://doi.org/10.1016/j.chempr.2022.08.004>.
- Barnard, E., Rubio Arias, J.J., and Thielemans, W. (2021). Chemolytic depolymerisation of PET: A review. *Green Chem.* 23, 3765–3789. <https://doi.org/10.1039/D1GC00887K>.
- Kosloski-Oh, S.C., Wood, Z.A., Manjarrez, Y., de los Rios, J.P., and Fieser, M.E. (2021). Catalytic methods for chemical recycling or upcycling of commercial polymers. *Mater. Horiz.* 8, 1084–1129. <https://doi.org/10.1039/D0MH01286F>.
- Shukla, S.R., and Kulkarni, K.S. (2002). Depolymerization of poly(ethylene terephthalate) waste. *J. Appl. Polym. Sci.* 85, 1765–1770. <https://doi.org/10.1002/app.10714>.
- Jehanno, C., Flores, I., Dove, A.P., Müller, A.J., Ruipérez, F., and Sardon, H. (2018). Organocatalysed depolymerisation of PET in a fully sustainable cycle using thermally stable protic ionic salt. *Green Chem.* 20, 1205–1212. <https://doi.org/10.1039/C7CG03396F>.
- Liu, Y., Yao, X., Yao, H., Zhou, Q., Xin, J., Lu, X., and Zhang, S. (2020). Degradation of poly(ethylene terephthalate) catalyzed by metal-free choline-based ionic liquids. *Green Chem.* 22, 3122–3131. <https://doi.org/10.1039/D0GC00327A>.
- Fan, C., Zhang, L., Zhu, C., Cao, J., Xu, Y., Sun, P., Zeng, G., Jiang, W., and Zhang, Q. (2022). Efficient glycolysis of PET catalyzed by a metal-free phosphazene base: the important role of EG⁻. *Green Chem.* 24, 1294–1301. <https://doi.org/10.1039/D1GC03885K>.
- Zhou, L., Lu, X., Ju, Z., Liu, B., Yao, H., Xu, J., Zhou, Q., Hu, Y., and Zhang, S. (2019). Alcoholysis of polyethylene terephthalate to produce diethyl terephthalate using choline chloride-based deep eutectic solvents as efficient catalysts. *Green Chem.* 21, 897–906. <https://doi.org/10.1039/C8GC03791D>.
- Bartolome, L., Imran, M., Lee, K.G., Sangalang, A., Ahn, J.K., and Kim, D.H. (2014). Superparamagnetic γ -Fe₂O₃ nanoparticles as an easily recoverable catalyst for the chemical recycling of PET. *Green Chem.* 16, 279–286. <https://doi.org/10.1039/C3GC41834K>.
- Yang, R.-X., Bieh, Y.-T., Chen, C.H., Hsu, C.-Y., Kato, Y., Yamamoto, H., Tsung, C.-K., and Wu, K.C.W. (2021). Heterogeneous metal azolate framework-6 (MAF-6) catalysts with high zinc density for enhanced polyethylene terephthalate (PET) conversion. *ACS Sustainable Chem. Eng.* 9, 6541–6550. <https://doi.org/10.1021/acssuschemeng.0c08012>.
- Du, J.-T., Sun, Q., Zeng, X.-F., Wang, D., Wang, J.-X., and Chen, J.-F. (2020). ZnO nanodispersion as pseudohomogeneous catalyst for alcoholysis of polyethylene terephthalate. *Chem. Eng. Sci.* 220, 115642. <https://doi.org/10.1016/j.ces.2020.115642>.
- Yao, H., Liu, L., Yan, D., Zhou, Q., Xin, J., Lu, X., and Zhang, S. (2022). Colorless BHET obtained from PET by modified mesoporous catalyst ZnO/SBA-15. *Chem. Eng. Sci.* 248, 117109. <https://doi.org/10.1016/j.ces.2021.117109>.
- Zhang, M., Averseng, F., Haque, F., Borghetti, P., Krafft, J.-M., Baptiste, B., Costentin, G., and Stankic, S. (2019). Defect-related multicolour emissions in ZnO smoke: from violet, over green to yellow. *Nanoscale* 11, 5102–5115. <https://doi.org/10.1039/C8NR09998G>.
- Wang, X., Zhang, Y., Si, H., Zhang, Q., Wu, J., Gao, L., Wei, X., Sun, Y., Liao, Q., Zhang, Z., et al. (2020). Single-atom vacancy defect to trigger high-efficiency hydrogen evolution of MoS₂. *J. Am. Chem. Soc.* 142, 4298–4308. <https://doi.org/10.1021/jacs.9b12113>.
- Jiang, W., Low, J., Mao, K., Duan, D., Chen, S., Liu, W., Pao, C.-W., Ma, J., Sang, S., Shu, C., et al. (2021). Pd-modified ZnO–Au enabling alkoxy intermediates formation and dehydrogenation for photocatalytic conversion of methane to ethylene. *J. Am. Chem. Soc.* 143, 269–278. <https://doi.org/10.1021/jacs.0c10369>.
- Zhu, S., Li, X., Pan, Z., Jiao, X., Zheng, K., Li, L., Shao, W., Zu, X., Hu, J., Zhu, J., et al. (2021). Efficient photooxidation of methane to liquid oxygenates over ZnO nanosheets at atmospheric pressure and near room temperature. *Nano Lett.* 21, 4122–4128. <https://doi.org/10.1021/acs.nanolett.1c01204>.
- Ou, G., Xu, Y., Wen, B., Lin, R., Ge, B., Tang, Y., Liang, Y., Yang, C., Huang, K., Zu, D., et al. (2018). Tuning defects in oxides at room temperature by lithium reduction. *Nat. Commun.* 9, 1302. <https://doi.org/10.1038/s41467-018-03765-0>.
- Lei, F., Sun, Y., Liu, K., Gao, S., Liang, L., Pan, B., and Xie, Y. (2014). Oxygen vacancies confined in ultrathin indium oxide porous sheets for promoted visible-light water

- splitting. *J. Am. Chem. Soc.* **136**, 6826–6829. <https://doi.org/10.1021/ja501866r>.
29. Xue, X., Chen, R., Chen, H., Hu, Y., Ding, Q., Liu, Z., Ma, L., Zhu, G., Zhang, W., Yu, Q., et al. (2018). Oxygen vacancy engineering promoted photocatalytic ammonia synthesis on ultrathin two-dimensional bismuth oxybromide nanosheets. *Nano Lett.* **18**, 7372–7377. <https://doi.org/10.1021/acs.nanolett.8b03655>.
30. Kim, H.-S., Cook, J.B., Lin, H., Ko, J.S., Tolbert, S.H., Ozolins, V., and Dunn, B. (2017). Oxygen vacancies enhance pseudocapacitive charge storage properties of MoO_{3-x} . *Nat. Mater.* **16**, 454–460. <https://doi.org/10.1038/nmat4810>.
31. Geng, Z., Kong, X., Chen, W., Su, H., Liu, Y., Cai, F., Wang, G., and Zeng, J. (2018). Oxygen vacancies in ZnO nanosheets enhance CO_2 electrochemical reduction to CO. *Angew. Chem. Int. Ed.* **57**, 6054–6059. <https://doi.org/10.1002/anie.201711255>.
32. Chen, S., Wang, H., Kang, Z., Jin, S., Zhang, X., Zheng, X., Qi, Z., Zhu, J., Pan, B., and Xie, Y. (2019). Oxygen vacancy associated single-electron transfer for photofixation of CO_2 to long-chain chemicals. *Nat. Commun.* **10**, 788. <https://doi.org/10.1038/s41467-019-08697-x>.
33. Gao, S., Sun, Z., Liu, W., Jiao, X., Zu, X., Hu, Q., Sun, Y., Yao, T., Zhang, W., Wei, S., and Xie, Y. (2017). Atomic layer confined vacancies for atomic-level insights into carbon dioxide electroreduction. *Nat. Commun.* **8**, 14503. <https://doi.org/10.1038/ncomms14503>.
34. Dong, J.J., Zhang, X.W., You, J.B., Cai, P.F., Yin, Z.G., An, Q., Ma, X.B., Jin, P., Wang, Z.G., and Chu, P.K. (2010). Effects of hydrogen plasma treatment on the electrical and optical properties of ZnO films: Identification of hydrogen donors in ZnO. *ACS Appl. Mater. Interfaces* **2**, 1780–1784. <https://doi.org/10.1021/am100298p>.
35. Wei, X.Q., Man, B.Y., Liu, M., Xue, C.S., Zhuang, H.Z., and Yang, C. (2007). Blue luminescent centers and microstructural evaluation by XPS and Raman in ZnO thin films annealed in vacuum, N_2 and O_2 . *Phys. B Condens. Matter* **388**, 145–152. <https://doi.org/10.1016/j.physb.2006.05.346>.
36. Chen, X., Li, Y., Pan, X., Cortie, D., Huang, X., and Yi, Z. (2016). Photocatalytic oxidation of methane over silver decorated zinc oxide nanocatalysts. *Nat. Commun.* **7**, 12273. <https://doi.org/10.1038/ncomms12273>.
37. Cho, S., Jang, J.-W., Lee, J.S., and Lee, K.-H. (2010). Exposed crystal face controlled synthesis of 3D ZnO superstructures. *Langmuir* **26**, 14255–14262. <https://doi.org/10.1021/la102126m>.
38. Liang, M.-K., Limo, M.J., Sola-Rabada, A., Roe, M.J., and Perry, C.C. (2014). New insights into the mechanism of ZnO formation from aqueous solutions of zinc acetate and zinc nitrate. *Chem. Mater.* **26**, 4119–4129. <https://doi.org/10.1021/cm501096p>.
39. Dong, J.-Y., Hsu, Y.-J., Wong, D.S.-H., and Lu, S.-Y. (2010). Growth of ZnO nanostructures with controllable morphology using a facile green antisolvent method. *J. Phys. Chem. C* **114**, 8867–8872. <https://doi.org/10.1021/jp102396f>.
40. McLaren, A., Valdes-Solis, T., Li, G., and Tsang, S.C. (2009). Shape and size effects of ZnO nanocrystals on photocatalytic activity. *J. Am. Chem. Soc.* **131**, 12540–12541. <https://doi.org/10.1021/ja9052703>.
41. Zhang, M., Zhou, W., Hu, W., Li, B., Qiao, Q., and Yang, S. (2020). Controlled formation of native defects in ultrapure ZnO for the assignment of green emissions to oxygen vacancies. *J. Phys. Chem. C* **124**, 12696–12705. <https://doi.org/10.1021/acs.jpcc.0c01078>.
42. Sheetz, R.M., Ponomareva, I., Richter, E., Andriotis, A.N., and Menon, M. (2009). Defect-induced optical absorption in the visible range in ZnO nanowires. *Phys. Rev. B* **80**, 195314. <https://doi.org/10.1103/PhysRevB.80.195314>.
43. Song, H., Meng, X., Wang, S., Zhou, W., Wang, X., Kako, T., and Ye, J. (2019). Direct and selective photocatalytic oxidation of CH_4 to oxygenates with O_2 on cocatalysts/ZnO at room temperature in water. *J. Am. Chem. Soc.* **141**, 20507–20515. <https://doi.org/10.1021/jacs.9b11440>.
44. Jehanno, C., Demarteau, J., Mantione, D., Arno, M.C., Ruipérez, F., Hedrick, J.L., Dove, A.P., and Sardon, H. (2021). Selective chemical upcycling of mixed plastics guided by a thermally stable organocatalyst. *Angew. Chem. Int. Ed.* **60**, 6710–6717. <https://doi.org/10.1002/anie.202014860>.
45. Kresse, G., and Furthmüller, J. (1996). Efficiency of ab-initio total energy calculations for metals and semiconductors using a plane-wave basis set. *Comput. Mater. Sci.* **6**, 15–50. [https://doi.org/10.1016/0927-0256\(96\)00008-0](https://doi.org/10.1016/0927-0256(96)00008-0).
46. Surendranath, Y., Kanan, M.W., and Nocera, D.G. (2010). Mechanistic studies of the oxygen evolution reaction by a cobalt-phosphate catalyst at neutral pH. *J. Am. Chem. Soc.* **132**, 16501–16509. <https://doi.org/10.1021/ja106102b>.
47. Perdew, J.P., Burke, K., and Ernzerhof, M. (1997). Generalized gradient approximation made simple. *Phys. Rev. Lett.* **77**, 1396. <https://doi.org/10.1103/PhysRevLett.77.1396>.
48. Henkelman, G., Uberuaga, B.P., and Jónsson, H. (2000). A climbing image nudged elastic band method for finding saddle points and minimum energy paths. *J. Chem. Phys.* **113**, 9901–9904. <https://doi.org/10.1063/1.132967>.

STAR★METHODS

KEY RESOURCES TABLE

REAGENT or RESOURCE	SOURCE	IDENTIFIER
Chemicals, peptides, and recombinant proteins		
Zinc chloride	Sigma-Aldrich	208086: CAS_7646-85-7
ammonium bicarbonate	Sigma-Aldrich	A6141: CAS_1066-33-7
Ethylene glycol	Sigma-Aldrich	324558: CAS_107-21-1
L-asparagine	Sigma-Aldrich	A0084: CAS_70-47-3
Zinc oxide	Sigma-Aldrich	544906: CAS_1314-13-2
Copper oxide	Sigma-Aldrich	544868: CAS_1317-38-0
Tricobalt tetroxide	Sigma-Aldrich	637025: CAS_1308-06-1
Nickel oxide	Sigma-Aldrich	637130: CAS_1313-99-1
Iron oxide	Sigma-Aldrich	544884: CAS_1309-37-1
Ceria	Sigma-Aldrich	700290: CAS_1306-38-3
Aluminum oxide	Sigma-Aldrich	544833: CAS_1344-28-1
Silica	Sigma-Aldrich	748161: CAS_7631-86-9
Cetyltrimethylammonium bromide	Sigma-Aldrich	H5882: CAS_57-09-0
Software and algorithms		
Vienna ab initio simulation package	Kresse and Furthmüller ⁴⁵	https://doi.org/10.1016/0927-0256(96)00008-0
ChemDraw Professional 18.0	PerkinElmer	https://www.perkinelmer.com/category/chemdraw

RESOURCE AVAILABILITY

Lead contact

Further information and requests for resources should be directed to and will be fulfilled by the lead contact, Dr. Wei Jiang (jiangwei@nju.edu.cn).

Materials availability

This study did not generate new materials.

Data and code availability

- All data reported in this paper will be shared by the [lead contact](#) upon request.
- This paper does not report the original code.
- Any additional information required to reanalyze the data reported in this paper is available from the [lead contact](#) upon request.

METHOD DETAILS

Materials

Zinc chloride (ZnCl₂, CA>99%), ammonium bicarbonate (NH₄HCO₃, AR), and ethylene glycol (EG, AR) were purchased from Sigma-Aldrich Chemical Reagent Co., Ltd. Zinc oxide (ZnO), copper oxide (CuO), tricobalt tetroxide (Co₃O₄), nickel oxide (NiO, 30 nm, CA> 99.5%), iron oxide (Fe₂O₃), ceria (CeO₂), aluminum oxide (Al₂O₃), silica (SiO₂) were purchased from Sigma-Aldrich and used as the catalyst. All the chemical reagents were analytical grade and were used without further purification. Ultrapure water was used in all experiments.

Synthesis of ZnO NSs

ZnO nanosheets were synthesized using a two-step method. First, ZnCl₂ (20 mM) and NH₄HCO₃ (20 mM) were mixed in a round-bottom flask. The mixed solution was stirred for 2 h at a reaction temperature of

70°C, and the white precipitates were separated by centrifugation and were dried (80°C) overnight. Afterward, the precursors were calcined in a furnace in the air at 350°C for 1 h.

Synthesis of ZnO NRs

Firstly, 2.720 g zinc chloride was added into a 250 mL flask filled with 150 mL water and stirred for 10 min, then 0.320 g of L-asparagine was added and stirred for 30 min. Sodium hydroxide (1.500 g) was dissolved in 50 mL water in a beaker, and the solution was slowly dropped into the flask and stirred for 2 h. The flask was transferred to a water bath with a temperature of 95°C for reflux for 6 h. Afterward, the reactants were cooled to room temperature, the products were separated by centrifugation, and washed with water three times. The product was transferred to a vacuum drying oven set at 70°C for overnight drying. The pyrolysis method of ZnO NEs is consistent with that of ZnO NSs.

Synthesis of ZnO NEs

Firstly, 2.720 g zinc chloride was added into a 250 mL flask filled with 150 mL water. The mixture was stirred for 10 min, then 1.200 g CTAB was added into the flask and stirred for 30 min. Sodium hydroxide (1.500 g) was dissolved in a 100 mL beaker containing 50 mL water. The sodium hydroxide solution was slowly dropped into the mixed solution in the flask and stirred for 2 h. The flask was transferred to a water bath set at 95°C for reflux for 6 h. After cooling to room temperature, the product was separated by centrifugation, and washed with water and ethanol three times, and the precipitates were transferred to a vacuum drying oven set at 70°C for overnight drying. The pyrolysis method of ZnO NEs is consistent with that of ZnO NSs.

Evaluation of the catalytic glycolysis of PET with ZnO

Approximately 1.0 g of waste PET or commercial PET (Mw=27750; PD=1.9; particle size 450 μm) and an appropriate amount of catalyst and EG (4.0 g) were mixed in a single-neck flask at atmospheric pressure. The reaction was performed in reaction atmospheres of air, O₂, and N₂ and was carried out in an oil bath at 160°C-190°C. The catalytic reaction time ranged from 10 to 90 min. For comparison, studies on the effect of different metal oxide materials were conducted.

Approximately 400 mL of distilled water was added to the filtrate, and then the solution was heated at 70°C with magnetic stirring. After the solution became clear with a few floccules, the hot solution was quickly filtered. The filter cake consisted of oligomers, and the filtrate was a mixture of the remaining ethylene glycol, catalyst, monomer, and distilled water. The filtrate was diluted to 1000 ml with distilled water in a volumetric flask. The PET conversion and BHET yield are defined as Equations 1 and 2, respectively:

$$\text{Conv.}_{(PET)}\% = \frac{W_{PET} - W_{undepolymerized - PET}}{W_{PET}} \quad (\text{Equation 1})$$

$$\text{Yield.}_{(BHET)}\% = \frac{n_{BHET}}{n_{initial - PET}} \quad (\text{Equation 2})$$

Therefore, we describe the PET conversion force as the mass of PET that was depolymerized divided by the total mass of the PET [Equation 1]. The BHET production was calculated by dividing the number of obtained moles of BHET by moles of PET [Equation 2].

Space-Time Yield (STY) calculation

As a typical example, for 10 mg of ZnO, the moles of the product after a 1 h reaction was calculated based on the amount of BHET produced. Thus, the STY value was calculated via Equation 3:

$$\text{STY}_{(BHET)} \left(n_{BHET} \cdot g_{cat}^{-1} \cdot h^{-1} \right) = \frac{n_{BHET}}{m_{cat} * 1} \quad (\text{Equation 3})$$

Carbon balance

$$\text{Carbon balance} = \frac{n(\text{output of BHET, EG and dimer})}{n(\text{input of PET})} \times 100\%$$

In most cases, there was no PET left, meaning the conversion was 100%. Meanwhile, the carbon balance was $100\% \pm 3\%$, when the recycling and separation process was not performed, so the selectivity generally equaled yield.

Catalyst recycling

For the catalyst recycling test, the freshly reduced catalyst (ZnO, 50 nm), ethylene glycol, and PET (particle size = $450 \mu\text{m}$, $M_n = 192 \text{ g mol}^{-1}$) were loaded into a 25 mL Sylvie reactor at atmospheric pressure. The PET depolymerization was carried out at 180°C for 1 h. The catalyst was recovered and then calcined in the flowing air at 400°C for 2 h to remove the dimer. The phase structure before and after regeneration was verified by XRD (Figure 3B). The calcined catalyst was reduced again under the flow of H_2 (5 vol% in Ar, 50 mL/min) at 350°C for 2 h to obtain recycled catalysts. The purpose of using H_2 was to increase the O_v on the surface of ZnO. This recycled catalyst was loaded with ethylene glycol and PET into a 25 mL glass reactor, and the reaction was conducted again at 180°C for 1 h. The same recovery/regeneration procedure was repeated.

Catalyst of characterization

To analyze the bulk phase composition and crystallite structure of the catalysts, XRD patterns were obtained using a Bruker D8 Advance diffractometer (40 kV, 40 mA) with a $\text{Cu K}\alpha$ radiation source ($\lambda = 1.5406 \text{ \AA}$) and 2θ values between $10^\circ \sim 80^\circ$. Raman spectra of the ZnO catalysts were collected in a range of 100 to 800 cm^{-1} using Renishaw with an excitation wavelength of 532 nm. TEM images were obtained on a JEOL-2010 electron microscope at an acceleration voltage of 200 kV. The HRTEM images were obtained with a JEOL JEM-ARM200F instrument using a spherical aberration corrector. Room-temperature ESR spectra were obtained using a JEOL JES-FA200 ESR spectrometer (300 K, 9.062 GHz). Room temperature photoluminescence (PL) spectra were obtained by using a Jobin Yvon Fluorolog 3-TAU luminescence spectrometer (Jobin Yvon Instruments Co., Ltd., France). XPS spectra were obtained using a PerkinElmer PHI 1600 ESCA system with an $\text{Al K}\alpha$ radiation source at 1486.7 eV as the excitation source. The spectra were collected at ambient temperature under an ultrahigh vacuum. The binding energy (BE) scale was measured based on the standard C 1s peak of graphite at 284.6 eV.

Analysis of starting materials and products

Differential scanning calorimetry (DSC)

The melting point of PET and BHET was analyzed by DSC (TA instruments Discovery) measurements. The test method: temperature from -90°C to 160°C (300°C), and a heating rate of $10^\circ\text{C}/\text{min}$ under a nitrogen atmosphere.

Fourier transforms infrared (FTIR) spectroscopy. The FTIR spectra of PET and BHET have been recorded on a Nicolet iS5 FT-IR (Thermo Fisher) spectrometer at a single attenuated total reflectance (ATR) mode. IR spectra were measured with a resolution of 1.0 cm^{-1} over the range $400\text{--}4000 \text{ cm}^{-1}$. The air background was subtracted from the spectrum for each sample.

High-performance liquid chromatography (HPLC)

BHET and dimer were analyzed quantitatively on a Dionex HPLC-U3000 measured with a C18 column ($5 \mu\text{m}$, $250 \times 4.6 \text{ mm}^2$, Agilent) and a UV detector at 254 nm. The mobile phase was methanol/water ($v/v = 50/50$) for the running time of 10 min at 30°C , the flow rate of 0.5 mL min^{-1} , and the injection volume of $10 \mu\text{L}$.

NMR spectroscopy

^1H NMR and ^{13}C NMR spectra of BHET were recorded using a Varian Unity Inova AS600 spectrometer in a $\text{DMSO-}d_6$ solution. ^1H NMR (400 MHz, 298 K) spectra were analyzed using MestReNova (v11.0.1, Mestrelab Research S. L.): δ 8.12 (s, 4H, CH), 4.96 (t, $J = 5.70 \text{ Hz}$, 2H, -OH), 4.32 (t, $J = 4.90 \text{ Hz}$, 4H, -OCH₂), 3.72 (t, $J = 5.2 \text{ Hz}$, 4H, -CH₂-OH). ^{13}C NMR spectra were acquired on a Bruker AVANCE III Ultrashield Plus 800 MHz (18.8 T) spectrometer, and were analyzed using MestReNova (v11.0.1, Mestrelab Research S. L.). A Bruker TXI HCN cryoprobe was used to enhance sensitivity for direct ^{13}C detection. ^{13}C spectra were recorded using a long relaxation delay (10 s) to ensure quantitative intensities. ^{13}C NMR (100 MHz): δ 165.20 (2C, C=O), 133.7 (2C, -C-C=O), 129.50 (4C, CH), 67.00 (2C, O-CH₂), 58.98 (2C, CH₂-OH). Chemical shifts (δ , ppm) were calibrated using the residual proton signals of the solvent and were referenced to tetramethylsilane (TMS).

Gel permeation chromatography (GPC)

Molecular weight distributions of the pristine PET or the oligomer were analyzed on an Agilent PL-GPC 220 gel permeation chromatographer, equipped with a PL-Gel Mixed B guard column, three PL-Gel Mixed B columns, and a refractive index (RI) detector. PET was dissolved in hexafluoroisopropanol, and the oligomer was dissolved in dichloromethane.

In situ FTIR

Operando FTIR measurements were performed by using an *in situ* IR spectrograph (Mettler-Toledo-ReactIR) equipped with a ReactIR 10 and an MCT detector and a probe connected via a K6 Conduit (16 mm probe). Sampling was conducted within a wavenumber resolution range of 4000 to 650 cm^{-1} . ZnO (50 mg) and PET (2.0 g) were added to EG (8.0 g), reaction conditions (180°C for 2 h, 1 atm). After reaching the reaction temperature equilibrium (10 min) in the air atmosphere, the spectra were collected. Each spectrum was recorded by averaging 128 scans at a resolution of 2 cm^{-1} . Finally, the background was subtracted from the obtained spectra, which were collected during 5 min of reaction.

DFT calculation details

The first-principles calculations were carried out with the Vienna ab initio simulation package.^{45,46} The interaction between the ions and the valence electrons is described using projector augmented wave (PAW) potentials, and the exchange-correlation between electrons is treated by using the generalized gradient approximation (GGA) in the Perdew-Burke-Ernzerhof (PBE) form.⁴⁷ DFT-D3 method was employed to calculate the van der Waals (vdW) interaction. To achieve the accurate density of the electronic states, the plane wave cutoff energy was 480 eV, and a $4 \times 2 \times 1$ for sheet k-point mesh was used. Ionic relaxations were carried out under the conventional energy (10-4 eV) and force (0.01 eV/Å) convergence criteria. The ZnO slab with 8 atom layers along the [002] projection was used to mimic the as-prepared ZnO NRs, and ZnO NSs was simulated by constructing the [100] ZnO slab, where in cases a 1.5 nm vacuum layer was added to avoid the interaction between the adjacent layers.

The formation energy of oxygen vacancy and zinc vacancy in the corresponding slabs can be calculated according to the following formula (here we only take the neutral defect into account):

$$E(\sigma)f = E(\sigma - \text{vacancy}) - \sum n_{\sigma}\mu_{\sigma} - E(\text{slab}) \quad (\text{Equation 4})$$

where $E(\sigma)f$ represents the formation energy of σ (O or Zn) vacancy, $E(\sigma\text{-vacancy})$ is the calculated energy of O or Zn-vacancy ZnO slab, μ_{σ} is the chemical potential and n_{σ} represents the number of defects ($n < 0$ for removing atoms). $E(\text{slab})$ means the calculated energy of pure ZnO or defect ZnO slab. The chemical potential can be calculated as follows:

$$\mu_{\text{Zn}} + \mu_{\text{O}} = E(\text{ZnO}_{\text{bulk}}) \quad (\text{Equation 5})$$

in which μ_{Zn} and μ_{O} are related to the reaction conditions. For Zn-rich conditions, $\mu_{\text{Zn}} = E(\text{Zn}_{\text{bulk}})$ and $\mu_{\text{O}} = E(\text{ZnO}_{\text{bulk}}) - \mu_{\text{Zn}}$. For O-rich conditions, $\mu_{\text{O}} = 1/2 E(\text{O}_{2\text{gas}})$ and $\mu_{\text{Zn}} = E(\text{ZnO}_{\text{bulk}}) - \mu_{\text{O}}$.

Gibbs free energies for O_2 activation were calculated at 298.15 K, according to the expression:

$$G = E_{\text{DFT}} + E_{\text{ZPE}} - TS \quad (\text{Equation 6})$$

where E_{DFT} is the electronic energy calculated with VASP, E_{ZPE} is the zero-point energy, TS is the entropy contribution. Standard ideal gas methods were employed to compute E_{ZPE} and TS from temperature, pressure, and calculated vibrational energies. We added 6 molecules of ethylene glycol to mimic the reaction conditions with the solvent density of 1.11 g/cm^3 . All 3N degrees of freedom were treated as frustrated harmonic vibrations with negligible contributions from the catalyst surfaces for adsorbates. The transition state search was conducted with the climbing image nudged elastic band (CI-NEB) method, followed by the dimer method to converge the saddle point within 0.05 eV/Å.⁴⁸